MATERIALS SCIENCE

Heterojunction structures for reduced noise in large-area and sensitive perovskite x-ray detectors

Ying Zhou, Liang Zhao, Zhenyi Ni, Shuang Xu, Jingjing Zhao, Xun Xiao, Jinsong Huang*

Polycrystalline perovskites can be readily fabricated into large areas using solution depositions; however, they suffer from large dark currents that are tens to hundreds times higher than industrially relevant values, limiting their application in low-dose x-ray detection. Here, we show that the application of a heterojunction structure into polycrystalline films significantly reduces the dark current density by more than 200 times to subnanoampere per square centimeter without reducing the sensitivity of the detectors. The heterojunction perovskite films are formed by laminating several membrane films filled with perovskites of different bandgaps. A gradient bandgap is formed during annealing. The detectors have a lowest detectable dose rate of 13.8 ± 0.29 nGy_{air} s^{-1} for 40-keV x-ray and can conduct dynamic x-ray imaging at a low-dose rate of 32.2 nGy_{air} s^{-1}. Simulation and experimental analysis show that the heterojunction is tolerant of halide diffusion and can be stable for over 15 years.

INTRODUCTION

Metal halide perovskites (MHPs) have been shown to be excellent candidate materials for highly sensitive x-ray detectors with their extraordinary detection properties, including high stopping power to x-ray, large mobility-lifetime (μτ) products, tunable bandgap, low density of excess free charge carriers, and high photoluminescence (PL) quantum efficiencies (*1*–*8*). Comparing to the state-of-the-art x-ray detectors using amorphous selenium (α-Se) whose sensitivity drops quickly when x-ray energy goes above 30 keV, MHPs are much more sensitive to hard x-rays (*9*). MHPs can be easily fabricated through a low-temperature solution process, which makes them compatible with Si-based application-specific integrated circuits for signal readout (*10*). In recent years, highly sensitive perovskite ionization radiation detectors have been developed in direct or indirect (scintillator) detection modes. Because dominant indirect x-ray detectors using scintillators coupled with photodetector arrays have a limited spatial resolution due to the cross-talk between pixels (*11*), direct MHPs x-ray detectors are particularly attractive due to their capability to further increase the detection resolution and sensitivity (*12*). High sensitivity can reduce x-ray dose to patients in medical x-ray imaging, which makes perovskite x-ray detectors outstanding among all existing technologies (*13*). Both single crystalline and polycrystalline perovskites have been applied in these x-ray detectors (*1*, *14*–*16*). A notable amount of efforts have been devoted to enhancing the sensitivity of the perovskite x-ray detectors in the past few years; however, there are very few studies on the noise behavior of the perovskite detectors. Similar to weak light sensors, the lowest detectable x-ray dose is determined by the dark current of the devices, in addition to the responsivity (*17*, *18*). A large gain in photoconductive type detectors may give a large responsivity but does not necessarily enhance the capability of the weak light detection, because the dark current can be large in the photoconductive type devices. Despite of the very low sensitivity of 20 μC Gy_{air}^{-1} cm^{-2} for α-Se due to the very small μτ products, their extremely small dark current at the level of 1 nA cm^{-2} still allows them to be used for medical x-ray imaging to detect weak x-ray signals (*19*–*21*).

Department of Applied Physical Science, University of North Carolina at Chapel Hill, Chapel Hill, NC 27599, USA.
*Corresponding author. Email: jhuang@unc.edu

Most of current perovskite x-ray detectors rely on the bulk resistivity of perovskites for a low dark current based on the ohmic law of $J = E/\rho$, where J is dark current density, E is applied electric field intensity, and ρ is bulk resistivity. In this context, perovskite single crystals have advantages over polycrystalline films with much lower densities of extrinsic doping and charge traps, mainly because of the tremendously lower defect density (*2*, *5*). However, the reported resistivities of the state-of-the-art perovskite bulk crystals with most compositions are still too low to ensure a low dark current. Most optimized perovskite single crystals have a bulk resistivity in the order of 10^{10} ohm·cm or less (*1*, *15*, *22*), which would give a dark current of 50 nA cm^{-2} in devices operating even at a low electric field of 0.05 V μm^{-1}. It is still 50 to 500 times higher than the acceptable dark current limit in a direct-conversion flat-panel x-ray imagers of 0.1 to 1 nA cm^{-2} (*23*). Another bigger challenge comes from a lack of established method yet to grow large-area and thin single crystals to meet real-world applications. Large-area MHPs polycrystalline films can be quickly deposited by low-cost solution processes, such as blade coating, ink-jet printing, or infiltration processes (*18*, *24*, *25*). However, all reported MHP polycrystalline detectors had large dark current densities of 50 to 500 nA cm^{-2} at an electrical field of 0.05 V μm^{-1}, which is already unexpectedly small considering their much more defective structures compared to single crystals (*16*, *26*, *27*). It is noted that the noise of a radiation detector is generally dominated by dark current, although other types of noise might also present (*13*). The large dark currents would reduce the imaging capability of MHP detectors under weak x-ray, which annuls the most attractive advantage of using MHPs for x-ray medical imaging to reduce x-ray dose to patients (*28*).

In this work, we report heterojunction structure perovskites to reduce the dark current density of polycrystalline perovskite devices by over 200 times without compromising their sensitivity. The perovskite heterojunction was formed by laminating membranes filled with perovskite of different bandgaps, which allows them to be scalable and flexible. A gradient composition was also formed to guide photogenerated charges transport. We demonstrated that the heterojunction x-ray detectors have a dark current comparable to that of the optimized α-Se detectors but are ~800 times more sensitive, which enables them to capture clear x-ray images at a very low-dose rate of 32.2 nGy_{air} s^{-1}, and can image with ~1000 times weaker dose to the patient.

RESULTS

Heterojunction devices design and fabrication

Our method to reduce the dark current of the device under reverse bias is to introduce a heterojunction by inserting a wider bandgap (WBG) perovskite between the regular perovskite and electrode, as illustrated in Fig. 1 (A and B), because the inserted WBG perovskite layer can block the hole or electron injection due to a larger energy barrier. We simulated the dark current of the devices with structures shown in Fig. 1 (A and B) using the solar cell capacitance simulator (SCAPS), and the result is shown in Fig. 1C. Here, we assumed ohmic contacts at both perovskite-electrode interfaces, and the bandgaps of narrower bandgap layer and WBG layer are set to be 1.52 and 2.04 eV, respectively. Other simulation details can be found in the Supplementary Materials. The dark current curve of the heterojunction device exhibits a clear rectification, while the device with single composition perovskite shows a symmetrical dark current curve under forward and reverse biases. The heterojunction device has two orders of magnitude lower dark current under reverse bias, despite that the trap density of the inserted WBG layer was set to be three orders of magnitude larger than that of the single composition perovskite.

It is challenging to achieve a large-area heterojunction film using all solution methods, while vacuum deposition method can be time-consuming or expensive, because medical imaging needs perovskites of large area up to 43 cm by 43 cm with a thickness in millimeter scale (*29*). Fortunately, this is enabled by our recently demonstrated large-area perovskite-filled membrane films, in which MHP microcrystals are loaded into membranes by a simple and scalable solution infiltration (*18*). Here, we changed to a dip coating process and found that MHPs could infiltrate into the membranes as well. The compositions and thus the bandgaps of the loaded MHPs can be easily tuned by this method. As illustrated in Fig. 1D, free-standing heterojunction films with a total thickness of ~520 μm were fabricated by laminating five layers of $Cs_{0.15}FA_{0.85}PbI_3$-filled nylon membranes and a layer of $Cs_{0.15}FA_{0.85}Pb(I_{0.15}Br_{0.85})_3$-filled nylon membrane at elevated temperatures, where FA is formamidinium ($CH_2CHNH_2^+$). Here, MA (methylammonium)-free mixed cation perovskites were chosen, because they are much more stable under light and at high temperature (*30*). This simple fabrication method can make large-area and uniform heterojunction perovskite films. Ultraviolet photoelectron spectroscopy measurement shows that $Cs_{0.15}FA_{0.85}PbI_3$ and $Cs_{0.15}FA_{0.85}Pb(I_{0.15}Br_{0.85})_3$ have valance band maximum (VBM) levels of −6.12 and −6.14 eV, respectively, and the work functions of the $Cs_{0.15}FA_{0.85}PbI_3$ and $Cs_{0.15}FA_{0.85}Pb(I_{0.15}Br_{0.85})_3$ are 5.23 and 5.22 eV, respectively (fig. S1). The optical bandgaps of $Cs_{0.15}FA_{0.85}PbI_3$ and $Cs_{0.15}FA_{0.85}Pb(I_{0.15}Br_{0.85})_3$ are 1.55 and 2.07 eV, respectively. An energy diagram can then be constructed for the heterojunction devices operating under reverse bias, which is shown in Fig. 1F. The energy

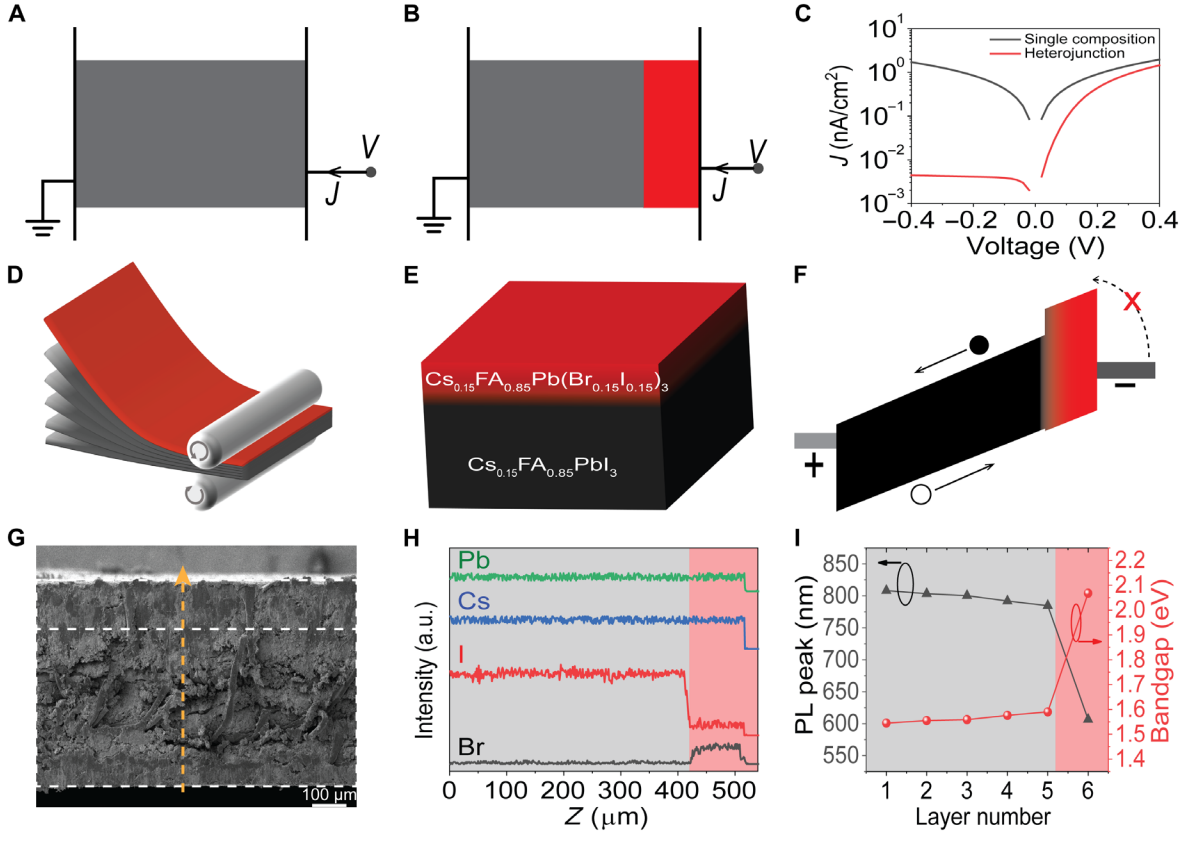

Fig. 1. Heterojunction perovskite devices design, fabrication, and characterization. Devices structure of single composition device (**A**) and heterojunction device (**B**) used in SCAPS simulation. Gray color represents a narrower bandgap perovskite, and the red color represents a WBG perovskite. (**C**) Simulated *J-V* curves for single composition and heterojunction perovskite device. (**D**) Perovskite-filled membrane film lamination scheme. (**E**) Heterojunction perovskite film structure scheme. (**F**) Band diagram of the heterojunction perovskite film. (**G**) Cross-sectional SEM image of the heterojunction perovskite film. (**H**) EDS linear scanning along the yellow line in (G). a.u., arbitrary units. (**I**) Location-dependent PL peak and bandgap, the layer number is from the bottom $Cs_{0.15}FA_{0.85}PbI_3$ layer to the top $Cs_{0.15}FA_{0.85}Pb(I_{0.15}Br_{0.85})_3$ layer.

diagram shows a large electron injection barrier (~1.0 eV) when high work function conductors, such as carbon, are used as the anode, which results in a significantly reduced dark current. The cross-sectional scanning electron microscopy (SEM) image shows that the heterojunction perovskite films were very dense without any pin holes or voids, and all the layers were connected well with each other physically without notable gaps between the layers. The energy-dispersive x-ray spectroscopy (EDS) linear scanning reveals that lead and cesium were uniformly distributed throughout the laminated film, and bromide only presented in the top 100-μm-thick layer. The signal intensity of iodide in the top 100-μm-thick layer was 18% of those in other layers, which is consistent with the loaded perovskite compositions.

Because a high temperature annealing process was applied during the film fabrication process, we speculate the halide ions should diffuse, particularly when the films were not fully dried, which should cause a composition gradient. To evaluate it, we measured the PL spectra of the films at different depth by peeling off the perovskite films layer by layer. The mechanically strong membrane allows each layer to be peeled off with maintained integrity, as shown by the photograph in fig. S2. The PL spectrum of each layer has only one peak with a symmetrical shape, indicating no phase separation in each layer (fig. S3). The PL peaks of the six layers from the bottom $Cs_{0.15}FA_{0.85}PbI_3$ layer to top $Cs_{0.15}FA_{0.85}Pb(I_{0.15}Br_{0.85})_3$ layer were located at 808.3, 803.5, 800.5, 791.9, 784.7, and 606.5 nm, respectively (Fig. 1I). Ultraviolet-visible absorption spectra of the six layers were also measured to determine their optical bandgaps. The optical bandgap of the top $Cs_{0.15}FA_{0.85}Pb(I_{0.15}Br_{0.85})_3$ layer is 2.07 eV, and the bandgap of the $Cs_{0.15}FA_{0.85}PbI_3$ layers gradually increased from 1.55 to 1.59 eV as they approached the $Cs_{0.15}FA_{0.85}Pb(I_{0.15}Br_{0.85})_3$ layer (fig. S4), implying that there was a diffusion of bromide during the lamination process into other layers and thus formed gradient bandgaps. As illustrated by the energy diagram in Fig. 1F, the gradient junction can guide the transport of photogenerated charges so that they can be efficiently collected by the electrodes.

Heterojunction material optoelectronic properties

The laminated heterojunction films were fabricated as x-ray detectors with a configuration of chromium (Cr)/bathocuproine (BCP)/C_{60}/perovskite film/carbon, as illustrated in Fig. 2A. Here, we used carbon materials as electrode, which was reported to be compatible with perovskites without chemical or electrochemical reactions (*31*). The carbon electrodes were deposited by blading commercial carbon paste onto the perovskite films, producing large-area electrodes at a high speed. At the same time, devices with a single composition of $Cs_{0.15}FA_{0.85}PbI_3$ were fabricated using the same structure as control, in which the 500-μm-thick perovskite films were prepared by laminating six layers of $Cs_{0.15}FA_{0.85}PbI_3$-filled membrane films. Figure 2B presents typical current density voltage (*J-V*) curves of the control and heterojunction devices. In the absence of light, the dark current curve of the heterojunction device exhibited an obvious rectification, while the dark current curve was almost symmetrical for

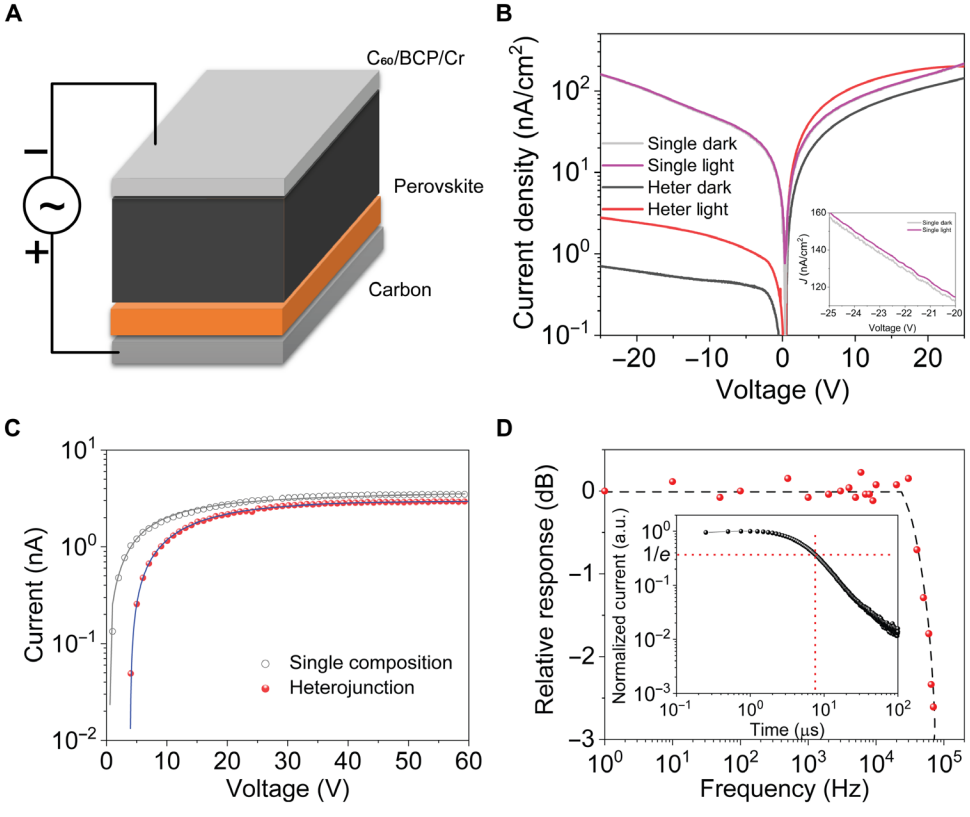

Fig. 2. Performance of heterojunction perovskite devices. (**A**) Heterojunction device structure scheme. (**B**) *J-V* curves of the single composition and heterojunction devices, and the inset is the partially enlarged *J-V* curves of the single composition device. (**C**) μτ product derived by fitting the steady-state photocurrent-bias curves with the modified Hecht equation. (**D**) Normalized response as a function of input light frequency, and inset is the transit time measured by transient photocurrent.

the control device under forward and reverse biases. The dark current density of the heterojunction device was reduced to 0.701 nA cm^{-2} at an operation bias of −25 V, in contrast to the >200 times larger dark current of 158.1 nA cm^{-2} in the control device at the same bias. Dark current stability under operation conditions is equally important for low-dose x-ray detection. In this context, we kept the device under a fixed bias (−25 V) at room temperature for 7 hours and monitored the dark current drift, and we found barely any dark current drift, as shown in fig. S5. This indicates that ion drift is not obvious in these condensed films under regular operating conditions. The x-ray–induced current densities under the same dose rate of 1.21 $\mu Gy_{air}\ s^{-1}$ were 2.32 and 2.05 nA cm^{-2} from the control and heterojunction devices under a bias of −25 V, respectively. The comparable x-ray generated current density indicates that heterojunction does not sacrifice the charge collection efficiency.

The μτ product of the heterojunction perovskite was derived by fitting the steady-state photocurrent-bias curves with the modified Hecht equation (*32*), as shown in Fig. 2C. The derived μτ product of the heterojunction perovskite film was 8.47×10^{-3} $cm^2\ V^{-1}$, which is several times higher than that of passivated $Cs_2AgBiBr_6$ polycrystalline wafer (*16*) and is over 10 times larger than that of the best reported polycrystalline $MAPbI_3$ films (*25*). The μτ product of the heterojunction perovskite film is comparable to that of the control films with a single composition (9.06×10^{-3} $cm^2\ V^{-1}$), once again demonstrating that the heterojunction only reduces the dark current without affecting charge collection. The frequency dependent response of the heterojunction device was carried out with a commercial green color light-emitting diode (LED) as the light source, which was modulated by a signal generator to generate a square wave light intensity at a frequency up to 2 MHz. An oscilloscope was used to record the photocurrent of the device. The device's frequency response is shown in Fig. 2D, which was derived from the amplitude of the device photocurrent under different LED frequencies. The 3-dB cutoff frequency (f_{3dB}) was 72 kHz for the heterojunction device under a bias of −25 V. The corresponding transit time is estimated by $f_{3dB} \approx \frac{0.443}{\tau_{tr}}$ to be 6.1 μs, which excellently agreed with the measured transient time using the transient photocurrent method (inset of Fig. 2D).

X-ray detection and imaging using heterojunction devices

The x-ray response of the devices was first evaluated under x-ray with a peak energy of 60 keV, and the dose rate was tuned by changing the current of the x-ray tube or adding aluminum plates as filters. The current densities of both types of devices at various dose rates

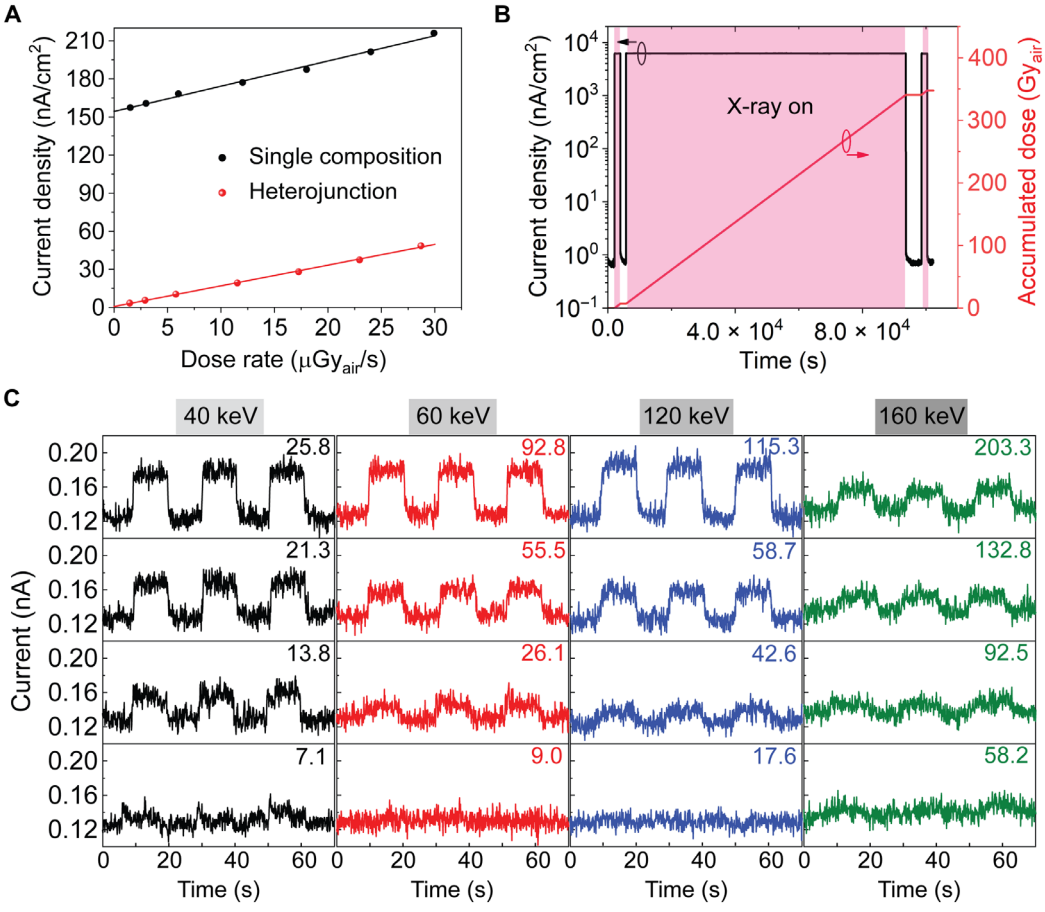

Fig. 3. X-ray detection performance of heterojunction perovskite devices. (**A**) Response of single composition and heterojunction perovskite detectors under −25 V bias. (**B**) Heterojunction device operation stability under a 60-keV x-ray with a dose rate of 3797 $\mu Gy_{air}\ s^{-1}$ for 1518 min. (**C**) The response of a heterojunction device to chopped 40-, 60-, 120-, and 160-keV x-rays with various dose rates under a bias of −25 V. The dose rates are added in each panel, and the unit is $nGy_{air}\ s^{-1}$. The turning on speed of signal is determined by the chopping rate.

are shown in Fig. 3A, and the responsivities of the detectors were derived from the slope of current density versus x-ray dose rate. The control and heterojunction detectors exhibited comparable responsivities of 1985 ± 72 μC Gy_{air}^{-1} cm^{-2} and 1629 ± 27 μC Gy_{air}^{-1} cm^{-2} under a small bias of −25 V, respectively, which is consistent with the charge collection properties. It is five times higher than that of indirect x-ray detectors using CsI:Tl scintillator (*33*). Because of the comparable dark current while much larger sensitivity, the heterojunction detectors exhibit ~800 times higher signal-to-noise ratio than α-Se detectors. We evaluated the operation stability of the heterojunction x-ray detector by irradiating the devices with 60-keV x-ray at a high dose rate of 3797 μGy_{air} s^{-1}, and a bias of −25 V was applied during the stress test to simulate the operating conditions. As shown in Fig. 3B, the dark current remained almost unchanged at 0.73 ± 0.05 nA cm^{-2} after irradiation for 1518 min. The accumulated dose reached 345.8 Gy_{air}, which is equivalent to 1.7 million posteroanterior chest examinations using the heterojunction perovskite detectors, considering that the entrance surface dose of chest radiography is 0.2 mGy_{air}.

The reduction of the dark current should allow the heterojunction device to detect weaker x-ray, if the devices maintain a linear response when the x-ray dose rate approaches noise equivalent power. To evaluate it, we measured the output current of the detectors under chopped x-ray by continuously reducing the x-ray dose rate, and we also did this measurement for x-rays with different peak energies to evaluate their potential application for hard x-ray detection. Figure 3C shows the collected current under x-rays of various energies and dose rates. With the reduction of the x-ray dose rate, the x-ray–induced signal became weaker and merged into noise. The current signal induced by 60-keV x-ray with a dose rate of 26.1 ± 0.54 nGy_{air} s^{-1} was distinguishable from the noise. When the x-ray peak energy went down slightly to 40 keV, the signal current generated by the x-ray at a dose rate of 13.8 ± 0.29 nGy_{air} s^{-1} was reliably distinguished from noise. On the other hand, the lowest detectable x-ray dose rate increased to 42.6 ± 1.05 nGy_{air} s^{-1} and 92.5 ± 1.76 nGy_{air} s^{-1} for hard x-rays with a peak energy of 120 and 160 keV, respectively. The different minimal x-ray dose rates under different x-ray energies can be explained by their percentage of x-ray stopped by the perovskite films.

To demonstrate the capability of heterojunction perovskite x-ray detectors for direct dynamic imaging at low-dose rate, we imaged a "UNC" logo made of lead vinyl using a heterojunction perovskite detector with a pixel size of 2 mm by 2 mm at different x-ray dose rates. Figure 4A shows images taken by the heterojunction perovskite detector under 60-keV x-rays with various dose rates. The UNC logo was very clear with a large signal-to-noise ratio when the dose rate was 4471 nGy_{air} s^{-1}, and the contrast decreased as the dose rate decreased. When the dose rate was reduced to 32.2 nGy_{air} s^{-1}, the UNC logo could still be clearly seen. For comparison, the UNC logo was blurred in the images taken by the control detector at a dose rate of 4471 nGy_{air} s^{-1}, and it could not be distinguished from noise when the dose rate was reduced to 98.7 nGy_{air} s^{-1}. Furthermore, to simulate the application of low-noise heterojunction perovskite x-ray detectors in security application, we concealed a metal wrench in a metal box and imaged the covered box under 60-keV x-rays with a low-dose rate of 98.7 nGy_{air} s^{-1}. The wrench inside the box was clearly revealed by the contrast that appeared in the image (Fig. 4C). We estimated the minimal dose-area product (DAP) of a

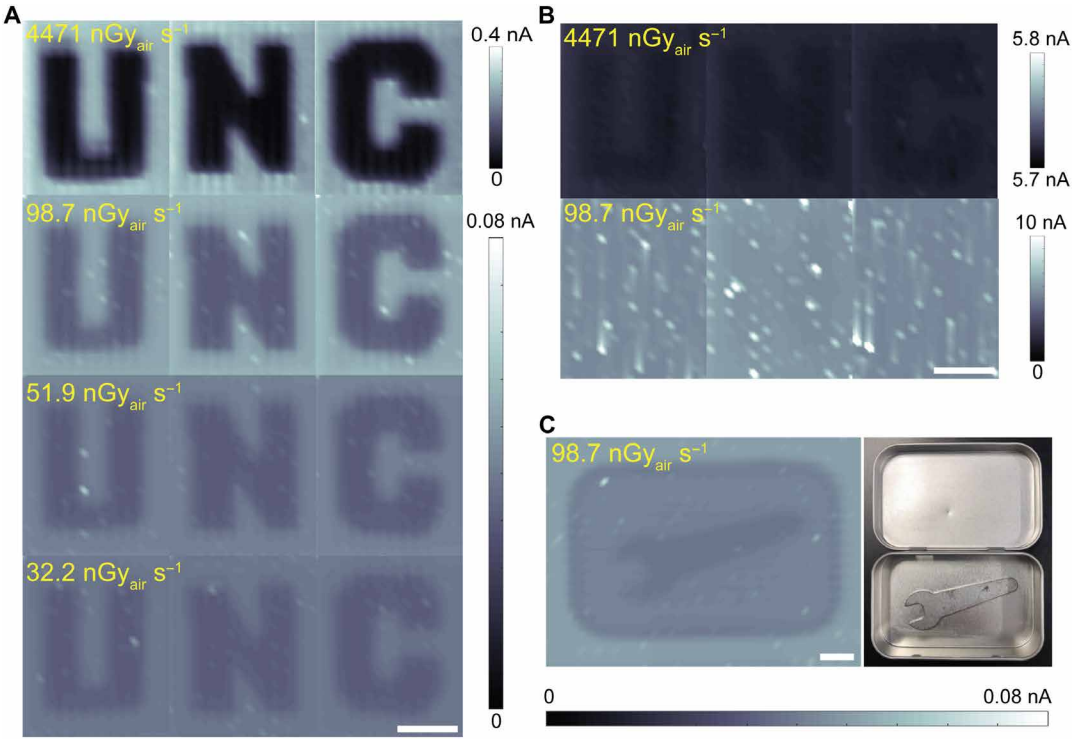

Fig. 4. X-ray imaging using different types of x-ray detectors. X-ray images of a UNC logo taken by a heterojunction perovskite device (**A**) and single composition perovskite device (**B**) under 60-keV x-rays with various dose rates. (**C**) X-ray image of a concealed metal wrench taken by heterojunction perovskite detector under 60-keV x-ray with a dose rate of 98.7 nGy_{air} s^{-1}, and right is the photograph. Scale bars, 20 mm. Photo credit: Ying Zhou, University of North Carolina at Chapel Hill.

posteroanterior chest (entrance area of 35 cm by 43 cm) test to patients based on the minimal dose rates these detectors can measure. Using the lowest x-ray dose rate reaching heterojunction perovskite detector (32.2 $nGy_{air}\ s^{-1}$) and an antennation of 97% after penetrating a 20-cm-thick human body (*34*), a minimal entrance surface dose rate of 1.07 $\mu Gy_{air}\ s^{-1}$ is derived. The calculated DAP is 0.157 $mGy_{air}\ cm^2$ by assuming an exposure period of 100 ms. This DAP is nearly three orders of magnitude less than the national diagnostic reference level of 0.15 Gy cm^2 (*35*).

Heterojunction device stability

One critical question arises whether the heterojunction structure can retain the small dark current for years, given that ion migration in polycrystalline perovskites has been shown to be nonnegligible in thin film perovskite solar cells (*36*). The abrupt heterojunction may change over time due to the interdiffusion of Br^- and I^- ions among the $Cs_{0.15}FA_{0.85}Pb(I_{0.15}Br_{0.85})_3$ and $Cs_{0.15}FA_{0.85}PbI_3$ layers. Here, both simulation and experiments were carried out to evaluate how ion diffusion affects heterojunction device performance. The distribution of Br^- ions in a 500-μm-thick film after Br diffusion at room temperature for 15 years was simulated on the basis of Fick's second law using a measured Br/I interdiffusion coefficient of $2.6 \times 10^{-12}\ cm^2\ s^{-1}$ at room temperature (*37*), and the simulation details can be found in the Supplementary Materials. As shown in Fig. 5A, the Br distribution changes an abrupt heterojunction into a gradient junction, after the devices are kept at room temperature for 15 years. The Br/(Br + I) ratios in the WBG perovskite layer decreases from 0.85 to 0.36, indicating that 57.6% of the Br in the $Cs_{0.15}FA_{0.85}Pb(I_{0.15}Br_{0.85})_3$ layer diffuse into the and $Cs_{0.15}FA_{0.85}PbI_3$ layers. Previous studies show that the Br/(Br + I) ratio and Cs^+ ratio dominate the conduction band minimum position of $Cs_yFA_{1-y}Pb(Br_xI_{1-x})_3$ but do not affect the VBM position (*38*–*40*). The bandgap of $FAPb(Br_xI_{1-x})_3$ varies almost linearly with the Br/(Br + I) ratio due to a small bowing factor (*41*). We can thus sketch the energy diagram for the heterojunction perovskites after halide diffuses at room temperature for 15 years and simulate the device dark current using SCAPS. Figure 5B shows that the dark current under reverse bias increases only by 35% compared to the pristine one, i.e., the dark current remains to be less than 1 nA cm^{-2} after 15 years of aging, indicating this heterojunction structure material is tolerant to halide diffusion. To verify it, encapsulated heterojunction perovskite devices were annealed at 70° to 150°C for 24 hours to accelerate the halide diffusion. As shown in Fig. 5C, the PL peaks of the bottom $Cs_{0.15}FA_{0.85}PbI_3$ layer and the top $Cs_{0.15}FA_{0.85}Pb(I_{0.15}Br_{0.85})_3$ layer barely changed after annealing at high temperatures. As shown in Fig. 5D, the dark current of these devices remained to be less than 1 nA cm^{-2}, and the responsivity was still larger than 1600 $\mu C\ Gy_{air}^{-1}\ cm^{-2}$, even after annealing at 150°C for 24 hours. Both simulation and experiments demonstrate that the heterojunction perovskite devices are tolerant of halide ion diffusion and thus are stable for long-term applications.

DISCUSSION

Low-noise, large-area, and highly sensitive x-ray detectors with heterojunction perovskite structure have been realized by laminating perovskite filled membranes with different compositions. The

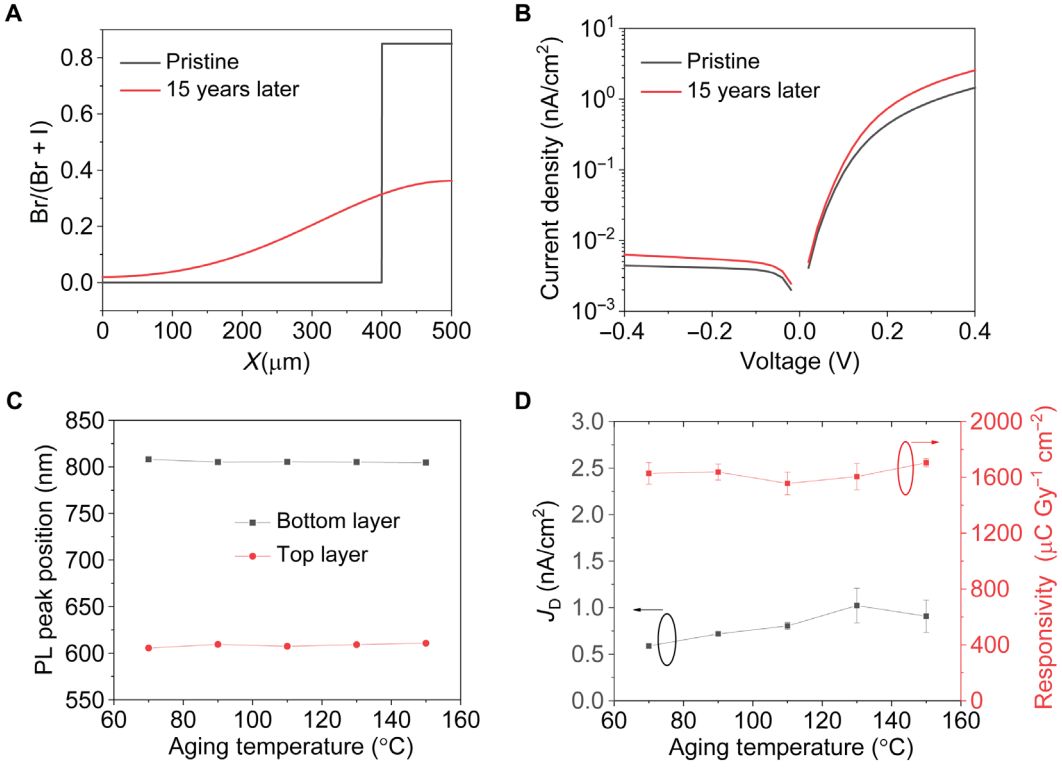

Fig. 5. Stability of heterojunction perovskite devices. (**A**) Simulation of Br distribution before and after diffusing at room temperature for 15 years, and (**B**) the corresponding *J-V* curves. (**C**) PL peak position of the bottom $Cs_{0.15}FA_{0.85}PbI_3$ layer and the top $Cs_{0.15}FA_{0.85}Pb(I_{0.15}Br_{0.85})_3$ layer after baking the encapsulated heterojunction devices. (**D**) Devices dark current density and sensitivity after aging at various temperatures for 24 hours (three devices for each temperature).

heterojunction reduces the dark current density of the polycrystalline x-ray detector by 200 times to 0.73 ± 0.05 nA cm^{-2}, which is comparable with that of optimized α-Se detectors, while the responsivity was not compromised. The low-noise and highly sensitive detectors can distinguish a lowest dose rate of 13.8 ± 0.29 nGy_{air} s^{-1} for 40-keV x-ray. The heterojunction detector could take clear dynamic x-ray imaging at a low-dose rate of 32.2 nGy_{air} s^{-1}, implying that the application of these low-noise heterojunction detectors can markedly reduce the x-ray dose exposed to patients by ~1000 times. This design makes the devices to be extremely robust both under x-ray, biasing, and long-term operation. The scalable fabrication strategy for fabricating large-area highly sensitive x-ray detectors with low dark and noise current will accelerate the commercialization of perovskites for direct x-ray imaging.

MATERIALS AND METHODS

Materials

Lead iodide (PbI_2, 99.99%) was purchased from Tokyo Chemical Industry (TCI). Dimethylformamide (DMF) and lead bromide ($PbBr_2$, >98%) were purchased from Alfa Aesar. FAI and FABr were purchased from GreatCell Solar. 2-Mercaptoethano (2-ME), dimethyl sulfoxide (DMSO), cesium iodide (CsI; 99.999%), and BCP (>96%) were purchased from Sigma-Aldrich. C_{60} (>99.55%) was purchased from Nano-C. Cr was purchased from K. J. Lesker. The nylon membranes were purchased from Sterlitech Corporation.

Device fabrication

FAI (17.6 mmol) and PbI_2 (17.6 mmol) were dissolved into 8 ml of 2-ME to obtain $FAPbI_3$ solution. $CsPbI_3$ solution was prepared by dissolving 4 mmol of CsI and 4 mmol of PbI_2 into 2 ml of DMSO. FABr (4.4 mmol) and $PbBr_2$ (4.4 mmol) were dissolved into 2 ml of DMF to obtain $FAPbBr_3$ solution. To obtain $Cs_{0.15}FA_{0.85}PbI_3$ solution, $CsPbI_3$ solution was added into $FAPbI_3$ solution with a Cs ratio of 15 mole percent (mol %). In addition, for $Cs_{0.15}FA_{0.85}Pb(I_{0.15}Br_{0.85})_3$ solution, $CsPbI_3$ solution was added into $FAPbBr_3$ solution with a Cs ratio of 15 mol %. In addition, 1 mol % $CdCl_2$ and 1 mol % FAI dissolved in 2-ME were added into the $Cs_{0.15}FA_{0.85}PbI_3$ solution and $Cs_{0.15}FA_{0.85}Pb(I_{0.15}Br_{0.85})_3$ solution as additive. The nylon membranes were immersed into the $Cs_{0.15}FA_{0.85}PbI_3$ solution or $Cs_{0.15}FA_{0.85}Pb(I_{0.15}Br_{0.85})_3$ solution for 15 to 20 min to maximize the loading of the perovskite solution in the membrane followed by annealing in a 160°C oven for 10 hours for solvent evaporation. Then, five layers of $Cs_{0.15}FA_{0.85}PbI_3$-filled membrane films and a layer of $Cs_{0.15}FA_{0.85}Pb(I_{0.15}Br_{0.85})_3$-filled membrane film were laminated at 170°C and 0 MPa for 10 min and then at 170°C and 2.5 MPa for 15 min. An MP170 900-W manual hydraulic rosin dab heat press machine was used for the laminating process. After lamination, carbon paste was bladed on one surface followed by annealing at 90°C for 90 min to evaporate the solvent of carbon paste. Then, 100 nm of C_{60}, 6 nm of BCP, and 50 nm of Cr were sequentially deposited on the other surface by thermal evaporation (Nexdep Angstrom), and the devices area is 0.18 cm^2.

Characterization

SEM was carried out using a FEI Helios 600 nanolab dual beam system. The 5 kV at low vacuum mode was applied for characterization. Linear EDS scanning was conducted using a Hitachi S-4700 cold cathode field emission scanning electron microscope with EDS. PL spectra were taken by a FluoTime 300 with an excitation wavelength of 485 nm and a 500-nm-long pass emission filter. X-ray detection measurements were carried out with a continuous x-ray source manufactured by COMET. The dose rate and peak energy of the x-ray were calibrated with a Raysafe X2 x-ray dosimeter, and the R/F sensor part was put side to the detectors during testing. The current of the devices was characterized by Keithley 2400 and 2601. All the detectors were characterized without encapsulation in the ambient atmosphere.

3 dB cutoff frequency measurement

The temporal response of the heterojunction perovskite device was measured using an Agilent 1-GHz digital oscilloscope (Agilent DSO-X-3140A), and the device was illustrated by 630-nm LED (LED supply) modulated by a function generator (Protek B8020FD 20-MHz DDS function generator) from the 20-nm semitransparent Cr electrode side. The rise and fall time of the LED measured by a 40-MHz Si PIN diode (Hamamatsu S3590-09) are 286.3 and 270.0 ns, respectively. The photogenerated weak current was amplified by a SR570 current preamplifier, which had a bandwidth of 1 MHz.

Photocurrent transit time

The device was illuminated by a 337-nm pulse laser with a pulse width of 4 ns from the 20-nm semitransparent Cr electrode side. The laser generated current was amplified by a SR570 current preamplifier and then recorded by a 1-GHz digital oscilloscope (Agilent DSO-X 3104A). The decay time is defined as the time the device takes to decay to 1/*e* of the initial signal intensity.

Single-pixel imaging

A detector with a size of 2 mm by 2 mm was placed under the imaging object, and the imaging object was driven by a program-controlled X-Y motion stage (Vexta pk 245-01AA X-Y scanning stage). During the imaging process, the weak x-ray generated current was amplified by a SR570 current preamplifier and then collected by the program developed by ourselves for imaging through a multifunction I/O device (NI USB-6229).

SUPPLEMENTARY MATERIALS

Supplementary material for this article is available at https://science.org/doi/10.1126/sciadv.abg6716

REFERENCES AND NOTES

1. H. Wei, Y. Fang, P. Mulligan, W. Chuirazzi, H.-H. Fang, C. Wang, B. R. Ecker, Y. Gao, M. A. Loi, L. Cao, J. Huang, Sensitive x-ray detectors made of methylammonium lead tribromide perovskite single crystals. *Nat. Photonics* **10**, 333–339 (2016).
2. Q. Dong, Y. Fang, Y. Shao, P. Mulligan, J. Qiu, L. Cao, J. Huang, Electron-hole diffusion lengths >175 μm in solution-grown $CH_3NH_3PbI_3$ single crystals. *Science* **347**, 967–970 (2015).
3. H. Wei, D. DeSantis, W. Wei, Y. Deng, D. Guo, T. J. Savenije, L. Cao, J. Huang, Dopant compensation in alloyed $CH_3NH_3PbBr_{3-x}Cl_x$ perovskite single crystals for gamma-ray spectroscopy. *Nat. Mater.* **16**, 826–833 (2017).
4. Y. Fang, Q. Dong, Y. Shao, Y. Yuan, J. Huang, Highly narrowband perovskite single-crystal photodetectors enabled by surface-charge recombination. *Nat. Photonics* **9**, 679–686 (2015).
5. D. Shi, V. Adinolfi, R. Comin, M. Yuan, E. Alarousu, A. Buin, Y. Chen, S. Hoogland, A. Rothenberger, K. Katsiev, Y. Losovyj, X. Zhang, P. A. Dowben, O. F. Mohammed, E. H. Sargent, O. M. Bakr, Low trap-state density and long carrier diffusion in organolead trihalide perovskite single crystals. *Science* **347**, 519–522 (2015).
6. Z. Ni, C. Bao, Y. Liu, Q. Jiang, W.-Q. Wu, S. Chen, X. Dai, B. Chen, B. Hartweg, Z. Yu, Z. Holman, J. Huang, Resolving spatial and energetic distributions of trap states in metal halide perovskite solar cells. *Science* **367**, 1352–1358 (2020).

7. Q. Chen, J. Wu, X. Ou, B. Huang, J. Almutlaq, A. A. Zhumekenov, X. Guan, S. Han, L. Liang, Z. Yi, J. Li, X. Xie, Y. Wang, Y. Li, D. Fan, D. B. L. Teh, A. H. All, O. F. Mohammed, O. M. Bakr, T. Wu, M. Bettinelli, H. Yang, W. Huang, X. Liu, All-inorganic perovskite nanocrystal scintillators. *Nature* **561**, 88–93 (2018).
8. M. Gandini, I. Villa, M. Beretta, C. Gotti, M. Imran, F. Carulli, E. Fantuzzi, M. Sassi, M. Zaffalon, C. Brofferio, L. Manna, L. Beverina, A. Vedda, M. Fasoli, L. Gironi, S. Brovelli, Efficient, fast and reabsorption-free perovskite nanocrystal-based sensitized plastic scintillators. *Nat. Nanotechnol.* **15**, 462–468 (2020).
9. Y. Liu, X. Zheng, Y. Fang, Y. Zhou, Z. Ni, X. Xiao, S. Chen, J. Huang, Ligand assisted growth of perovskite single crystals with low defect density. *Nat. Commun.* **12**, 1686 (2021).
10. W. Wei, Y. Zhang, Q. Xu, H. Wei, Y. Fang, Q. Wang, Y. Deng, T. Li, A. Gruverman, L. Cao, J. Huang, Monolithic integration of hybrid perovskite single crystals with heterogenous substrate for highly sensitive x-ray imaging. *Nat. Photonics* **11**, 315–321 (2017).
11. G. Spekowius, T. Wendler, *Advances in Healthcare Technology: Shaping the Future of Medical Care* (Springer Science & Business Media, 2006), vol. 6.
12. A. Smith, Fundamentals of digital mammography: Physics, technology and practical considerations. *Radiol. Manag.* **25 5**, 18–24, 26–31; quiz 32–14, (2003).
13. H. Wei, J. Huang, Halide lead perovskites for ionizing radiation detection. *Nat. Commun.* **10**, 1066 (2019).
14. R. Zhuang, X. Wang, W. Ma, Y. Wu, X. Chen, L. Tang, H. Zhu, J. Liu, L. Wu, W. Zhou, X. Liu, Y. Yang, Highly sensitive x-ray detector made of layered perovskite-like $(NH_4)_3Bi_2I_9$ single crystal with anisotropic response. *Nat. Photonics* **13**, 602–608 (2019).
15. W. Pan, H. Wu, J. Luo, Z. Deng, C. Ge, C. Chen, X. Jiang, W.-J. Yin, G. Niu, L. Zhu, L. Yin, Y. Zhou, Q. Xie, X. Ke, M. Sui, J. Tang, $Cs_2AgBiBr_6$ single-crystal x-ray detectors with a low detection limit. *Nat. Photonics* **11**, 726–732 (2017).
16. B. Yang, W. Pan, H. Wu, G. Niu, J.-H. Yuan, K.-H. Xue, L. Yin, X. Du, X.-S. Miao, X. Yang, Q. Xie, J. Tang, Heteroepitaxial passivation of $Cs_2AgBiBr_6$ wafers with suppressed ionic migration for x-ray imaging. *Nat. Commun.* **10**, 1989 (2019).
17. Y. Fang, A. Armin, P. Meredith, J. Huang, Accurate characterization of next-generation thin-film photodetectors. *Nat. Photonics* **13**, 1–4 (2019).
18. J. Zhao, L. Zhao, Y. Deng, X. Xiao, Z. Ni, S. Xu, J. Huang, Perovskite-filled membranes for flexible and large-area direct-conversion x-ray detector arrays. *Nat. Photonics* **14**, 612–617 (2020).
19. H. Huang, S. Abbaszadeh, Recent developments of amorphous selenium-based X-Ray detectors: A review. *IEEE Sensors J.* **20**, 1694–1704 (2020).
20. J. R. Scheuermann, A. H. Goldan, O. Tousignant, S. Léveillé, W. Zhao, Development of solid-state avalanche amorphous selenium for medical imaging. *Med. Phys.* **42**, 1223–1226 (2015).
21. D. M. Hunter, G. Belev, S. Kasap, M. J. Yaffe, Measured and calculated K-fluorescence effects on the MTF of an amorphous-selenium based CCD x-ray detector. *Med. Phys.* **39**, 608–622 (2012).
22. H. Li, J. Song, W. Pan, D. Xu, W.-a. Zhu, H. Wei, B. Yang, Sensitive and stable 2D perovskite single-crystal x-ray detectors enabled by a supramolecular anchor. *Adv. Mater.* **32**, 2003790 (2020).
23. S. Kasap, J. B. Frey, G. Belev, O. Tousignant, H. Mani, J. Greenspan, L. Laperriere, O. Bubon, A. Reznik, G. De Crescenzo, K. S. Karim, J. A. Rowlands, Amorphous and polycrystalline photoconductors for direct conversion flat panel x-ray image sensors. *Sensors* **11**, 5112–5157 (2011).
24. Y. Deng, C. H. Van Brackle, X. Dai, J. Zhao, B. Chen, J. Huang, Tailoring solvent coordination for high-speed, room-temperature blading of perovskite photovoltaic films. *Sci. Adv.* **5**, eaax7537 (2019).
25. Y. C. Kim, K. H. Kim, D.-Y. Son, D.-N. Jeong, J.-Y. Seo, Y. S. Choi, I. T. Han, S. Y. Lee, N.-G. Park, Printable organometallic perovskite enables large-area, low-dose x-ray imaging. *Nature* **550**, 87–91 (2017).
26. S. Shrestha, R. Fischer, G. J. Matt, P. Feldner, T. Michel, A. Osvet, I. Levchuk, B. Merle, S. Golkar, H. Chen, S. F. Tedde, O. Schmidt, R. Hock, M. Rührig, M. Göken, W. Heiss, G. Anton, C. J. Brabec, High-performance direct conversion x-ray detectors based on sintered hybrid lead triiodide perovskite wafers. *Nat. Photonics* **11**, 436–440 (2017).
27. W. Pan, B. Yang, G. Niu, K. H. Xue, X. Du, L. Yin, M. Zhang, H. Wu, X. S. Miao, J. Tang, Hot-pressed $CsPbBr_3$ quasi-Mmonocrystalline film for sensitive direct x-ray detection. *Adv. Mater.* **31**, 1904405 (2019).
28. D. J. Brenner, C. D. Elliston, E. J. Hall, W. E. Berdon, Estimated risks of radiation-induced fatal cancer from pediatric CT. *Am. J. Roentgenol.* **176**, 289–296 (2001).
29. J.-P. Moy, Recent developments in x-ray imaging detectors. *Nucl. Instrum. Methods Phys. Res. B* **442**, 26–37 (2000).
30. H. Wei, S. Chen, J. Zhao, Z. Yu, J. Huang, Is formamidinium always more stable than methylammonium? *Chem. Mater.* **32**, 2501–2507 (2020).
31. A. Mei, X. Li, L. Liu, Z. Ku, T. Liu, Y. Rong, M. Xu, M. Hu, J. Chen, Y. Yang, M. Grätzel, H. Han, A hole-conductor–free, fully printable mesoscopic perovskite solar cell with high stability. *Science* **345**, 295–298 (2014).
32. J. Androulakis, S. C. Peter, H. Li, C. D. Malliakas, J. A. Peters, Z. Liu, B. W. Wessels, J.-H. Song, H. Jin, A. J. Freeman, M. G. Kanatzidis, Dimensional reduction: A design tool for new radiation detection materials. *Adv. Mater.* **23**, 4163–4167 (2011).
33. G. Zentai, L. D. Partain, R. Pavlyuchkova, C. Proano, G. F. Virshup, B. N. Breen, A. I. Vilensky, O. Dagan, E. Meerson, M. Schieber, in *Smart Nondestructive Evaluation and Health Monitoring of Structural and Biological Systems II* (International Society for Optics and Photonics, 2003), vol. 5047, pp. 84–95.
34. P. Sprawls, *Physical Principles of Medical Imaging* (Aspen Publishers Gaithersburg, 1993).
35. D. Hart, M. Hillier, P. Shrimpton, Doses to patients from radiographic and fluoroscopic x-ray imaging procedures in the UK-2010 review. HPA-CRCE-034. *Health Protection Agency*, (2012).
36. Y. Yuan, J. Huang, Ion migration in organometal trihalide perovskite and its impact on photovoltaic efficiency and stability. *Acc. Chem. Res.* **49**, 286–293 (2016).
37. A. Osherov, Y. Feldman, I. Kaplan-Ashiri, D. Cahen, G. Hodes, Halide diffusion in $MAPbX_3$: Limits to topotaxy for halide exchange in perovskites. *Chem. Mater.* **32**, 4223–4231 (2020).
38. A. A. Zhumekenov, M. I. Saidaminov, M. A. Haque, E. Alarousu, S. P. Sarmah, B. Murali, I. Dursun, X.-H. Miao, A. L. Abdelhady, T. Wu, O. F. Mohammed, O. M. Bakr, Formamidinium lead halide perovskite crystals with unprecedented long carrier dynamics and diffusion length. *ACS Energy Lett.* **1**, 32–37 (2016).
39. K. T. Cho, S. Paek, G. Grancini, C. Roldán-Carmona, P. Gao, Y. Lee, M. K. Nazeeruddin, Highly efficient perovskite solar cells with a compositionally engineered perovskite/hole transporting material interface. *Energy Environ. Sci.* **10**, 621–627 (2017).
40. N. Li, Y. Luo, Z. Chen, X. Niu, X. Zhang, J. Lu, R. Kumar, J. Jiang, H. Liu, X. Guo, B. Lai, G. Brocks, Q. Chen, S. Tao, D. P. Fenning, H. Zhou, Microscopic degradation in formamidinium-cesium lead iodide perovskite solar cells under operational stressors. *Joule* **4**, 1743–1758 (2020).
41. Z. Muhammad, P. Liu, R. Ahmad, S. J. Asadabadi, C. Franchini, I. Ahmad, Tunable relativistic quasiparticle electronic and excitonic behavior of the $FAPb(I_{1-x}Br_x)_3$ alloy. *Phys. Chem. Chem. Phys.* **22**, 11943–11955 (2020).
42. M. Burgelman, P. Nollet, S. Degrave, Modelling polycrystalline semiconductor solar cells. *Thin Solid Films* **361**, 527–532 (2000).

Acknowledgments

Funding: This work was mainly financially supported by the University of North Carolina at Chapel Hill. We thank financial support for the characterization using x-ray from Defense Threat Reduction Agency (DTRA) under award HDTRA1-20-2-0002. **Author contributions:** J.H. conceived the idea. J.H. and Y.Z. designed experiments. Y.Z. and L.Z. fabricated the films and devices and characterized them. Z.N. conducted the *J-V* curves simulation. S.X. participated in the programming and diffusion simulation. Y.Z. and X.X. conducted in PL characterization. J.H. and Y.Z. wrote the manuscript and all authors reviewed it. **Competing interests:** J.H. and J.Z. are inventors on a patent application related to this work filed by University of North Carolina at Chapel Hill. All other authors declare that they have no competing interests. **Data and materials availability:** All data needed to evaluate the conclusions in the paper are present in the paper and/or the Supplementary Materials.

Submitted 20 January 2021
Accepted 12 July 2021
Published 1 September 2021
10.1126/sciadv.abg6716

Citation: Y. Zhou, L. Zhao, Z. Ni, S. Xu, J. Zhao, X. Xiao, J. Huang, Heterojunction structures for reduced noise in large-area and sensitive perovskite x-ray detectors. *Sci. Adv.* **7**, eabg6716 (2021).